



Universiteit
Leiden
The Netherlands

Semi-empirical approach to the simulation of molecule-surface reaction dynamics

Migliorini, D.

Citation

Migliorini, D. (2019, March 14). *Semi-empirical approach to the simulation of molecule-surface reaction dynamics*. Retrieved from <https://hdl.handle.net/1887/69724>

Version: Not Applicable (or Unknown)

License: [Licence agreement concerning inclusion of doctoral thesis in the Institutional Repository of the University of Leiden](#)

Downloaded from: <https://hdl.handle.net/1887/69724>

Note: To cite this publication please use the final published version (if applicable).

Cover Page



Universiteit Leiden



The handle <http://hdl.handle.net/1887/69724> holds various files of this Leiden University dissertation.

Author: Migliorini, D.

Title: Semi-empirical approach to the simulation of molecule-surface reaction dynamics

Issue Date: 2019-03-14

Chapter 2

Methods and Theory: A Semi-Empirical Approach to Density Functional Theory

Part of this Chapter is based on:

D. Migliorini *et al.*, *J. Chem. Phys. Lett.*, 8, 4177 (2017)

<https://pubs.acs.org/doi/abs/10.1021/acs.jpcllett.7b01905>

which is reproduced with the permission of ACS Publications¹.

2.1 Introduction

Heterogeneous catalysis generally focuses on very complicated processes that involve many molecular states and several reaction steps taking place on irregular and highly corrugated transition metal catalysts. Today an accurate simulation of such processes in their entirety is far beyond computational possibility. However it has been shown that usually only a very few of the molecular states involved exhibit a large degree of rate control on the overall process [1] and this allows experiments and simulations to focus on single fundamental steps rather than on

¹further permissions related to the material excerpted should be directed to the ACS.

the whole process. Often the catalytic system is modeled by a single reaction step involving a molecule dissociating on an ideal low-index metal surface.

Rate controlling states can be either molecular adsorption or transition states and they are crucial because a small change in their energy might dramatically affect the rate of the overall process. While molecular adsorption energies can be measured experimentally (i.e., using temperature programmed desorption), it is more complicated to design experiments able to measure dissociative chemisorption barriers. Theoretical calculations can provide energy barriers (E_b) but the large number of atoms and the periodic representation [2] needed for this kind of system makes accurate full quantum chemical simulations unfeasible. The theoretical method of choice to simulate the dissociation of molecules on a metal surface while including all the relevant atoms is density functional theory (DFT) at the generalized gradient approximation (GGA) level. Unfortunately GGA-DFT is not accurate enough to calculate chemically accurate barriers (i.e., with errors smaller than 1 kcal/mol \approx 4.2 kJ/mol) [3].

A way to improve DFT accuracy is to develop a semi-empirical specific reaction parameter (SRP) density functional. Recent theoretical work [4–6] and recent joint theoretical and experimental efforts [7, 8] have been successful in developing system-specific SRP functionals for several catalytically relevant systems [4–8] by comparing *ab initio* molecular dynamics (AIMD) simulations [9, 10] with supersonic molecular beam experiments.

In this Chapter the main steps needed to accurately simulate supersonic molecular beam experiments are reported and discussed in order to obtain an SRP functional for a polyatomic molecule dissociating on a transition metal surface. The Chapter is organized as follows: the basics of the DFT method and of the specific reaction parameter approach to DFT are explained in Section 2.2, the strategy to develop and test an SRP functional is reported in Section 2.3 and the procedure to accurately simulate molecular beam experiments is described in Section 2.4.

2.2 SRP Approach to DFT

DFT is a particularly convenient method to study catalytically relevant systems and surface science in general. The high complexity of these systems and the large number of degrees of freedom (DOFs) involved benefit from the favorable scaling of the computational cost of DFT ($\propto n^3$, where n is the total number of electrons), which is better than for correlated wavefunction-based methods. Moreover DFT offers an easy treatment of periodicity. This allows a full-dimensional treatment of larger systems (even for dynamical simulations, when coupled with classical time propagation), which are crucial to understand surface reactions. However this comes with the price of a lower accuracy due to the unknown analytical form of the exchange-correlation functional (E_{XC}), needed to obtain the energy of the system in the DFT approach. This problem of lack of accuracy for a molecule on a transition metal surface can be circumvented through a semi-empirical approach by developing a specific reaction parameter density functional (SRP-DFT).

2.2.1 Density Functional Theory

The heart of the DFT method is formed by the Hohenberg-Kohn theorems [11]. The first theorem states that for a non-degenerate ground state (gs) all the properties of the system are determined by the electronic density (ρ_0). This implies that the gs wave function ($\Psi_0(\mathbf{r}_1, \mathbf{r}_2, \dots, \mathbf{r}_n)$) can be expressed as a functional of the gs electronic density (ρ_0):

$$\Psi_0(\mathbf{r}_1, \mathbf{r}_2, \dots, \mathbf{r}_n) = \Psi[\rho_0(\mathbf{r})], \quad (2.1)$$

and allows one to write the gs expectation value of any observable \hat{O} as a functional of the density:

$$O_0 = O[\rho_0] = \langle \Psi[\rho_0(\mathbf{r})] | \hat{O} | \Psi[\rho_0(\mathbf{r})] \rangle. \quad (2.2)$$

This entails that the energy of the ground state is a functional of $\rho_0(\mathbf{r})$ as well. Moreover, the second Hohenberg-Kohn theorem states that, for a given system,

the energy $E[\rho']$ of a generic density ρ' cannot be lower than the gs energy $E[\rho_0]$:

$$E[\rho_0] = \langle \Psi[\rho_0(\mathbf{r})] | \hat{H} | \Psi[\rho_0(\mathbf{r})] \rangle \leq \langle \Psi[\rho'(\mathbf{r})] | \hat{H} | \Psi[\rho'(\mathbf{r})] \rangle = E[\rho'], \quad (2.3)$$

where \hat{H} is the Hamiltonian for the given system that can be written as:

$$\hat{H} = \hat{T} + \hat{U} + \hat{V}. \quad (2.4)$$

Here \hat{T} is the kinetic term, \hat{U} is the electron-electron interaction term and \hat{V} is the potential term due to the positively charged nuclei. In order to obtain the gs energy of the system, ideally one only has to minimize the functional:

$$E[\rho] = \langle \Psi[\rho] | \hat{T} + \hat{U} + \hat{V} | \Psi[\rho] \rangle. \quad (2.5)$$

However, in order to do so, analytical expressions for \hat{T} , \hat{U} and \hat{V} are needed.

The most common approach to solve the DFT problem and to obtain the gs energy has been proposed by Kohn and Sham [12]. The core idea of the Kohn-Sham (KS) method is to introduce a fictitious system of non-interacting particles that has the same gs density of the real interacting system and to solve a set of single-particle Kohn-Sham (KS) equations:

$$\left[-\frac{1}{2}\nabla^2 + V_s(\mathbf{r}) \right] \varphi_i(\mathbf{r}) = \epsilon_i \varphi_i(\mathbf{r}). \quad (2.6)$$

Here the gs wavefunction Ψ_0 has been written as a Slater determinant of single particle KS orbitals $\varphi_i(\mathbf{r})$, and $V_s(\mathbf{r})$ is the so-called KS potential. Equation 2.6 is reported in atomic units, consistently with the rest of the equations in this Section.

In order to solve the KS Equation 2.6, one can use the kinetic energy for a system of non-interacting particles $T_s[\rho]$, the Hartree interaction energy $U_H[\rho]$ (i.e., the coulombic repulsion), while moving the contributions due to the interacting nature of the system into the so-called exchange-correlation energy term

E_{XC} , so that:

$$E[\rho] = T_s[\rho] + U_H[\rho] + E_{XC}[\rho] + V[\rho], \quad (2.7)$$

where

$$E_{XC} = (U - U_H) + (T - T_s). \quad (2.8)$$

Note that Equation 2.7 is formally correct but the analytical expression of E_{XC} is unknown. Therefore, in order to obtain an accurate value for the energy, a good approximation (i.e., analytical expression) of E_{XC} is needed. Some of the most important and widely used approximations for E_{XC} are reported and discussed in Section 2.2.3. Now it is possible to define the KS potential as:

$$V_s(\mathbf{r}) = \int d\mathbf{r}' \frac{\rho(\mathbf{r}')}{|\mathbf{r} - \mathbf{r}'|} - \sum_N \frac{Z_N}{|\mathbf{r} - \mathbf{R}_N|} + V_{XC}(\mathbf{r}), \quad (2.9)$$

where the first term is the Hartree potential U_H , the second (V) is due to the interaction with the N nuclei in the system and $V_{XC}(\mathbf{r})$ is the derivative of $E_{XC}[\rho(\mathbf{r})]$ with respect to the density:

$$V_{XC}(\mathbf{r}) = \frac{\delta E_{XC}[\rho(\mathbf{r})]}{\delta \rho(\mathbf{r})}. \quad (2.10)$$

If V_s is defined as in Equation 2.9, from the solution of Equation 2.6 it is possible to recover the ground state density of the real correlated system as:

$$\rho_0(\mathbf{r}) = \sum_i f_i |\varphi_i(\mathbf{r})|^2. \quad (2.11)$$

where f_i are the occupation numbers. Note that $\rho_0(\mathbf{r})$ is the correct *gs* density if the exact analytical expression for E_{XC} would be known. The Kohn-Sham Equation 2.6 depend on the density $\rho(\mathbf{r})$ through $V_s(\mathbf{r})$ and $\rho(\mathbf{r})$ itself is obtained from the KS orbitals through Equation 2.11. Therefore, in order to optimize the KS orbitals $\varphi_i(\mathbf{r})$, the KS equations need to be solved self-consistently starting

from an initial guess of the density $\rho^{init}(\mathbf{r})$.

The KS approach shifts the problem from minimizing the energy functional to solving a set of non-interacting equations while, in principle, delivering the correct density ρ_0 (Equation 2.11) and energy $E[\rho_0]$ (Equation 2.7) of the real interacting and correlated system. As mentioned before, the overall accuracy of the method depends then on the quality of the approximation used to obtain the exchange-correlation contribution E_{XC} (see Section 2.2.3).

2.2.2 Plane Wave DFT

When it comes to describing periodic systems, it is possible to expand the KS orbitals according to Bloch's theorem in a set of plane waves that have the same periodicity as the system considered:

$$\varphi_j(\mathbf{r}, \mathbf{k}) = N \sum_{\mathbf{G}} c_{j\mathbf{G}\mathbf{k}} e^{i(\mathbf{k}+\mathbf{G})\mathbf{r}}. \quad (2.12)$$

Here j runs over the KS orbitals, \mathbf{k} is a vector in the irreducible Brillouin zone (IBZ), \mathbf{G} is a reciprocal lattice vector and N is a normalization constant. Equation 2.12 has to be solved for the coefficients $c_{j\mathbf{G}\mathbf{k}}$. Performing a plane wave DFT calculation requires two “parameters”: a grid of K-points in order to avoid having to integrate over all the IBZ, and a cut off on the kinetic energy of the plane waves (E_{cut}). This defines the size of the basis set as it will only include plane waves associated with a kinetic energy:

$$\frac{1}{2} |\mathbf{k} + \mathbf{G}|^2 \leq E_{cut}. \quad (2.13)$$

In order to obtain accurate results, the energy needs to be converged with respect to both the value of E_{cut} and the number of K-points.

In order to accurately reproduce the strongly oscillating wave function close to the nuclei one would need to use a very large value of E_{cut} , thus resulting in slowly converging calculations. This limitation can be circumvented by using pseudopotentials [13, 14] to explicitly treat only the valence electrons while re-

placing the strong Coulomb potential close to the nuclei with a weaker (effective) potential. This results in smoother wave functions close to the nuclei that can be described using a smaller value of E_{cut} , while approximately reproducing the all-electron wave functions at larger distances. Moreover the pseudopotentials can be designed to partially account for relativistic effects and, since only the chemically-relevant valence electrons are explicitly treated, they further reduce the calculation time.

The plane waves implementation of DFT has the advantage that the basis functions are inherently periodic and do not depend on the atomic positions but only on the size of the simulation box and on the value of E_{cut} . This avoids the basis-set superposition error (BSSE) and issues with systematic basis set convergence which are typical of atomic orbital based methods. On the other hand, it implies that increasing the box size will increase the computational cost even if the number of atoms is held constant. For surface simulations, this translates into a limitation of the size of the vacuum that can be used to separate the metal slab from its 1st periodic replica, which needs to be considered when long range interactions are included. A more detailed discussion is reported in Section 2.4.2.

2.2.3 Exchange-Correlation Functional

As mentioned before, the DFT approach is formally correct and it would return the exact ground state density and energy if an analytical expression for E_{XC} was known. Since the beginning of DFT, many different E_{XC} approximations have been proposed and applied to physically relevant systems. However the recipe for the universal exchange-correlation functional has not yet been found and any of the available approximations will perform better for some systems and worse for others.

The first form of E_{XC} is based on the assumption that the electrons behave as a homogeneous gas and it was proposed directly by Kohn and Sham [12] with

the name of local density approximation (LDA):

$$E_{XC}^{LDA}[\rho(\mathbf{r})] = \int \rho(\mathbf{r}) \epsilon_{xc}^{LDA}[\rho(\mathbf{r})] d\mathbf{r}, \quad (2.14)$$

where ϵ_{xc}^{LDA} can be decomposed into the exchange part ϵ_x [15, 16]:

$$\epsilon_x = -\frac{3}{4} \left(\frac{3}{\pi} \rho(\mathbf{r}) \right)^{1/3}, \quad (2.15)$$

and into the correlation part ϵ_c . The analytical expression of ϵ_c is known for the limits of high density (weak correlation) and low density (strong correlation). The two limits have then been connected by fitting results of Monte Carlo simulations [17].

The LDA approximation is based on the assumption that the electrons behave as a homogeneous gas and therefore it performs poorly when it comes to describe molecular bonds or molecule-surface interactions. This makes the LDA approximation not viable for heterogeneous catalysis where dissociation barrier heights are of fundamental importance and need to be calculated with high accuracy.

The next natural step to overcome the locality of this approximation is to include the gradient of the density ($\nabla\rho(\mathbf{r})$) in the expression of E_{XC} . The so-called semi-local generalized gradient approximation (GGA) functionals have a general form:

$$E_{XC}^{GGA}[\rho(\mathbf{r})] = \int \mathcal{F}[\rho(\mathbf{r}), \nabla\rho(\mathbf{r})] d\mathbf{r}, \quad (2.16)$$

where E_{XC}^{GGA} can be decomposed into the sum of the exchange part (E_X^{GGA}) plus the correlation part (E_C^{GGA}). Two of the most used GGA functionals in surface science are the Perdew-Burke-Ernzerhof (PBE) [18, 19] and its revised version by Nørskov and coworkers (RPBE) [20]. The PBE and the RPBE functionals have the same correlation part:

$$E_C^{GGA}[\rho(\mathbf{r})] = \int \rho(\mathbf{r}) \left(\epsilon_c[\rho(\mathbf{r})] + H[\rho(\mathbf{r}), \nabla\rho(\mathbf{r})] \right) d\mathbf{r}, \quad (2.17)$$

where the gradient contribution H is based on physical constraints.

For both PBE and RPBE the GGA exchange functional (E_X^{GGA}) has the general form:

$$E_X^{GGA}[\rho(\mathbf{r})] = \int \rho(\mathbf{r}) \epsilon_x[\rho(\mathbf{r})] F(s) d\mathbf{r}, \quad (2.18)$$

where $F(s)$ is the enhancement factor of the LDA ϵ_x and depends on the reduced density gradient $s(\mathbf{r})$:

$$s(\mathbf{r}) = \frac{|\nabla\rho(\mathbf{r})|}{[2(3\pi^2)^{1/3}\rho(\mathbf{r})^{4/3}]}. \quad (2.19)$$

The only difference between PBE [18] and RPBE [20] is in the expression of $F(s)$:

$$F^{PBE}(s) = 1 + k - \frac{k}{(1 + \mu s^2/k)}, \quad (2.20)$$

$$F^{RPBE}(s) = 1 + k(1 - e^{-\mu s^2/k}), \quad (2.21)$$

where k and μ are based on physical constants [18].

Several attempts have been made to improve further on the GGA approximation such as including the Laplacian of the electron density $\nabla^2\rho(\mathbf{r})$ (meta-GGA functionals) or adding fractions of the Hartree-Fock exchange (hybrid functionals). However these approximations are not suitable to effectively simulate molecules on surfaces due to, for instance, their high computational cost.

One of the pitfalls of the GGA approximation is that long range van der Waals interaction is not taken into account. Among the different approaches that have been proposed to overcome this limitation [21–24], one of the most interesting is the vdW-DF correlation functional developed by Dion *et al.* [24], which models the long range interaction based on the density of the system without semi-empirical parameters.

The vdW-DF approach consists in pairing a GGA exchange functional with a correlation ($E_C^{\text{vdW-DF}}$) that can model the van der Waals interaction. The ensuing correlation is defined as the sum of a local (LDA) part and a non local

(*nl*) contribution:

$$E_{XC}^{\text{vdW-DF}}[\rho(\mathbf{r})] = E_X^{\text{GGA}}[\rho(\mathbf{r})] + E_C^{\text{LDA}}[\rho(\mathbf{r})] + E_C^{\text{nl}}[\rho(\mathbf{r})], \quad (2.22)$$

where the non-local part of the correlation, which vanishes for a homogeneous density, is obtained through a double spatial integration over the density:

$$E_C^{\text{nl}}[\rho(\mathbf{r})] = \frac{1}{2} \iint d\mathbf{r}_1 d\mathbf{r}_2 \rho(\mathbf{r}_1) \Phi(q_1, q_2, r_{12}) \rho(\mathbf{r}_2). \quad (2.23)$$

The kernel Φ depends on $r_{12} = |\mathbf{r}_1 - \mathbf{r}_2|$ and on q_1 and q_2 which, in turn, depend on ρ and on $\nabla\rho$ evaluated in \mathbf{r}_1 and \mathbf{r}_2 .

Despite the complexity of $E_C^{\text{nl}}[\rho(\mathbf{r})]$, the kernel Φ can be tabulated and the integral can be very efficiently evaluated thanks to the implementation of Román-Pérez and Soler [25]. This makes the vdW-DF functional almost as fast to evaluate as any other standard GGA functional. Moreover the long range interaction is evaluated self-consistently on the density of the system without semi-empirical parameters [24, 26].

2.2.4 Specific Reaction Parameter Functional

The specific reaction parameter (SRP) approach to DFT is a semi-empirical method, originally proposed by Truhlar and coworkers [27]. Its implementation for molecules on surfaces allows us to develop a semi-empirical and system specific functional able to improve the accuracy of standard GGA functionals, which are in general not quantitative for these systems [3]. The SRP-DFT approach has been proven successful for different molecule-metal surface systems such as H_2 on Cu(111) [4], H_2 on Cu(100) [5], D_2 on Pt(111) [6] and recently CHD_3 on Ni(111) [7] and Pt(111) and Pt(211) [8]. The SRP strategy consists of selecting an experimental observable that depends on the minimum barrier height (i.e. the zero-coverage reaction probability S_0) and to choose two functionals that predict values that are systematically too high and too low compared to the experimental data. Note that the functionals of choice need to be able to reproduce

the shape of the reaction probability curve which depends on the distribution of energy barriers on the surface [28]. For many molecules reacting on a metal surface [4, 7, 8, 28–33] the GGA exchange functionals of choice are PBE [18] and RPBE [20], with the first known to usually underestimate and the second to overestimate barrier heights for these systems. The SRP exchange correlation functional (E_{XC}^{SRP}) is then defined as a linear combination of the chosen GGA functionals:

$$E_{XC}^{SRP} = x \cdot E_{XC}^{RPBE} + (1 - x) \cdot E_{XC}^{PBE}, \quad (2.24)$$

where x is an adjustable parameter that allows us to tune the performance of the functional in order to fit theoretical values of S_0 to a set of experimental results. Once the mixing parameter is identified, the SRP functional is tested and validated by simulating a different set of experimental data for the same system (more details are reported in Section 2.3).

The van der Waals interaction can be accounted for by replacing the PBE correlation functional present in PBE and RPBE by the vdW-DF correlation functional ($E_C^{\text{vdW-DF}}$) developed by Dion *et al.* [24, 25] and discussed in Section 2.2.3. This correlation functional has been shown to improve the description of weakly activated dissociation [28] while maintaining the same accuracy of [34], or improving the accuracy [7, 8] over that [33] achieved using Equation 2.24 for highly activated dissociation systems. Moreover, as mentioned before, the vdW-DF correlation functional is non-empirical being based on first principles [26]. The general formulation of the SRP functional used in most of the studies reported in this Thesis is based on a linear combination of the two GGA exchange functionals plus the vdW-DF correlation functional:

$$E_{XC}^{SRP} = x \cdot E_X^{RPBE} + (1 - x) \cdot E_X^{PBE} + E_C^{\text{vdW-DF}}. \quad (2.25)$$

The SRP functional is constructed as much as possible [7] on the basis of non-empirical, constrained-based functionals (including the spin-scaling relationship,

the Lieb-Oxford bound, and the recovery of the uniform gas limit [18, 24] that should ensure applicability to metals [35]).

2.3 Semi-Empirical Strategy

The strategy and the steps needed to develop and test an SRP functional for a polyatomic molecule dissociating on a metal surface are reported in the following Sections. The discussion is mainly focused on the tri-deuterated methane molecule (CHD_3) which has been the center of most of the studies on which this Thesis is based. However, the same methodology should be applicable, in principle, to any molecule dissociating on a transition metal surface through σ -bond breaking [8].

The SRP functional used in most of the work reported in this Thesis has been developed by comparing an observable that depends on the minimum barrier height, the zero-coverage reaction probability (S_0), obtained from *ab initio* molecular dynamics (AIMD) calculations [9, 10] and from supersonic molecular beam experiments. For specific initial conditions, S_0 can be measured experimentally using the King and Wells beam reflectivity technique [36, 37] after a molecular beam impinges on an ideal low-index metal surface. The same quantity can then be obtained from the number of reacted molecules (N_{react}):

$$S_0 = N_{react}/N_{tot}, \quad (2.26)$$

in a set of N_{tot} AIMD trajectories where a single molecule impinges on the surface, prepared as described in Section 2.4 to accurately reproduce the experimental initial conditions.

AIMD allows the accurate simulation of dynamical processes within the framework of the Born-Oppenheimer approximation. This approximation assumes that, due to the different time scale, it is possible to separate the motion of the electrons from that of the nuclei, effectively treating the electrons as if they were moving in the potential generated by the nuclei. For each propagation step

the energy and the forces are evaluated on-the-fly at a DFT level without the need to fit a high dimensional Potential Energy Surface (PES), and then the positions of the ions are classically propagated according to Newton's equations of motion. Moreover the quasi-classical trajectory (QCT) approach can be exploited by imparting vibrational zero-point energy (ZPE) to the molecule. For the experimental conditions addressed in this Thesis, AIMD-QCT is the method of choice to effectively simulate molecular beam experiments and to test the validity of the semi-empirical SRP approach. The main reason to choose AIMD over a higher level of theory (i.e., quantum dynamics) [38, 39] is the possibility to include explicitly all the DOFs of the system in the simulation without any dynamical approximation. Not only is it possible to include all the molecular DOFs, but the surface atom motion, which is known to be important for the dissociation of polyatomic molecules (such as methane) on metal surfaces [40], is also accounted for. AIMD can also be extended to reactions affected by electron-hole pair excitation by including electronic friction [41].

The results of the AIMD simulations are compared with experimental results for a set of laser-off conditions (for which the initial molecular rovibrational distribution only depends on the nozzle temperature, see Section 2.4) and, through a trial and error procedure, the parameter x of Equation 2.25 is optimized until the AIMD results are in agreement with the experiments within chemical accuracy. The agreement between the results is verified by fitting the experimental data and by checking that, on average, the distance on the energy axis from the AIMD results to the experimental fit is smaller than 4.2 kJ/mol. Once chemical accuracy has been reached for the laser-off simulations, the candidate SRP functional is validated by simulating a different experiment for the same system. The SRP functional presented in this Thesis has been tested against state-resolved molecular beam experiments for which the molecules impinge on the surface after being selectively prepared in a specific rovibrational state through laser excitation.

In order to ensure a meaningful comparison between experiments and AIMD-QCT simulations, many aspects have to be considered, both on the experimental and on the theoretical side. First, the total energy of the molecule (translational

+ vibrational) has to be chosen above the minimum ZPE corrected barrier. This ensures the applicability of the QCT approach because under such conditions the reaction occurs in the classical “over-the-barrier” regime [9, 42]. Second, the molecular beams have to be produced using a nozzle temperature (T_n) as low as possible, for example by taking advantage of H_2 seeding, so that most of the molecules are in the vibrational ground state. This limits the deficiencies of the QCT method in describing the reactivity of coupled excited vibrational states (i.e., the CD vibrational states in CHD_3) due to artificial intramolecular vibrational energy redistribution (IVR) caused by the availability of resonant vibrations [7]. For the same reason the $\nu_1 = 1$ excited state of CHD_3 is a good choice to compare theoretical and experimental state selected reaction probabilities. This excited vibrational state possesses 95% of CH stretch character [43] and, due to the lack of Fermi resonances, energy imparted to this normal mode in the gas-phase remains localized on a time scale comparable with the collision time [7, 8, 44]. The reactivity of $\nu_1 = 1$ CHD_3 is therefore unlikely to be affected by IVR [9, 44]. Third, the surface temperature (T_s) has to be chosen well above the Debye temperature T_D of the metal bulk, which varies with the composition of the surface. At T_s larger than T_D quantum effects are not expected to significantly affect the molecule-surface energy exchange dynamics, making such conditions suitable for AIMD simulations. Specifically, for values of T_s higher than the Debye-Waller temperature the validity of a classical approach to dynamics calculations on scattering from a surface can be assessed by computing the argument to the Debye-Waller factor [45]:

$$2W = \frac{3p^2 T_s}{M_C k_b T_D^2}, \quad (2.27)$$

where p^2 is the average of the square of the change in momentum of a scattering molecule, M_C the mass of a surface atom and k_b the Boltzmann constant. Experience suggests that treating the surface vibrations classically works well for $T_s > T_D$ for values of $2W$ greater than 6 [46, 47] (note that $2W$ is a dimensionless quantity) and that under such conditions, the energy transfer to the surface

phonons should happen classically. Finally AIMD cannot be comfortably used to compute reaction probabilities smaller than 1%. This is due to the high computational cost of the method which, in light of present-day computational resources, limits the number of trajectories (N_{tot}) that can be used to simulate a single beam condition to ≈ 500 -1000. This affects the accuracy of the results since the statistical error on S_0 representing the 68% confidence limits [48] depends on the reaction probability and on the total number of trajectories as:

$$\sigma_p = \sqrt{\frac{S_0(1 - S_0)}{N_{tot}}}. \quad (2.28)$$

This effectively reduces the statistical significance of low reaction probabilities computed with AIMD. However, once the SRP functional has been developed, in principle it is possible to couple it with an high dimensional PES approach that also describes the motion of the surface atoms (as demonstrated for $N_2 + Ru(0001)$ [49]) allowing the accurate simulation of smaller S_0 .

2.4 Initial Condition Sampling

In order to simulate a molecular beam experiment at an AIMD-QCT level it is important to accurately generate and sample the initial conditions of the system in order to have a fair comparison. In the work reported in this Thesis, we can distinguish between two classes of molecular beam experiments: laser-off and laser-on.

In laser-off experiments the molecules are accelerated according to the nozzle temperature (T_n) which defines the collision energy (E_i) distribution of the beam and the vibrational states as a Boltzmann distribution for that temperature. The rotational energy of the molecules is generally low as the number of intermolecular collisions during the expansion is high enough to dissipate it (rotational cooling). Therefore, in laser-off experiments, all the molecules are assumed to be in the rotational ground state. The experimental laser-off zero-coverage reactivity (S_0^{off}) can then be directly measured and so the molecules in the AIMD trajectories are

prepared to be randomly oriented, in the rotational ground state and sampling the experimental E_i distribution and all the vibrational states accessible at T_n .

In laser-on experiments an optical transition is used to excite molecules from an initial to a target rovibrational state and, since the laser excitation happens after the beam expansion (i.e., after rotational cooling), the molecules maintain the rotational excitation. A large fraction of the molecules is in the desired target state but a variety of other states are still present in the beam. However from the measured laser-on zero-coverage reaction probability (S_0^{on}) is possible to extract the reaction probability ($S_0^{\bar{v}}$) for the desired rovibrational state \bar{v} once S_0^{off} is known for the same E_i [50]. This can be evaluated as:

$$S_0^{\bar{v}} = \frac{S_0^{on} - S_0^{off}}{f_{exc}} + S_0^{v=0}, \quad (2.29)$$

where f_{exc} is the excited fraction, or the fraction of the molecule in the beam excited to the target state, and $S_0^{v=0}$ is the reaction probability of the ground state. $S_0^{v=0}$ can usually be approximated by S_0^{off} , which does result in a small overestimation. Other methods to estimate $S_0^{v=0}$ are available but it has been shown that, for systems like the ones addressed in this Thesis, they all give very similar results [7]. Being able to directly extract $S_0^{\bar{v}}$ from the experiments simplifies the simulations because it allows one to prepare all the molecules in the desired \bar{v} rovibrational state.

2.4.1 Molecular Beam

The initial conditions imparted to the projectile molecule need to accurately represent the experimental molecular beam that has to be modeled. In the experiments the molecules have a specific collision energy distribution and a specific rovibrational state associated with a defined angular momentum \mathbf{L} .

First of all the molecular beams simulated are very narrow in translational energy but not monochromatic. In order to describe the distribution of energies (and velocities) $n(E_i)$ of the beam, Michelsen and Auerbach [51] proposed the

expression:

$$n(E_i)dE_i = \frac{1}{N}E_i \exp \left[-4E_s \frac{(\sqrt{E_i} - \sqrt{E_s})^2}{(\Delta E_s)^2} \right] dE_i, \quad (2.30)$$

where the energy spread ΔE_s is defined by:

$$\frac{\Delta E_s}{E_s} \equiv \frac{2\alpha}{v_s}. \quad (2.31)$$

Here the stream velocity v_s and the width of the velocity distributions α can be obtained by fitting time of flight measurements [52]. Once v_s and α are available, the initial collision energy for the molecules in the trajectories is selected by sampling the distribution $n(E_i)$.

In order to prepare the molecule in the desired vibrational state the potential energy V_ν along each vibrational mode needs to be known. The vibrational modes can be obtained using finite differences as the eigenvectors of the mass-weighted Hessian and for each of them a one-dimensional potential is computed by displacing the molecule along the mode itself. This interpolation can be performed just once for each mode before preparing the whole set of molecules. Once the V_ν potentials are available the molecule can be prepared in the desired vibrational state.

In order to prepare a set of molecules in a target vibrational state (e.g., H_2O in $\nu_1=1, \nu_2=0, \nu_3=0$), one can perform a classical micro-canonical sampling for each mode of each molecule in the set. This is done by running a 1D quasi-classical dynamics simulation along each mode using the energy associated with the state we want to generate and then by randomly selecting the initial velocity (\mathbf{v}_{vib}) and displacement from the equilibrium positions ($\delta\mathbf{q}_{vib}$) from it (i.e., randomly selecting the phase of the vibration). The sum of the displacements and the velocities for all the modes is assigned to the molecule to prepare it in the target vibrational state. It is important to note that, since we sample the initial position classically along the vibrational modes and in the time domain, when we average over many generated molecules prepared in a given vibrational state we obtain

a classical distribution where the molecule has a higher probability to sit close to one of the turning points. Note that applying the shift $\delta\mathbf{q}_{vib}$ results in a small change in the inertia of the system and introduces small spurious rotational velocities which are computed and removed. If this correction changes the energy along the normal modes by more than 1 meV, the initial conditions are discarded and generated again from the beginning.

As mentioned before, molecules in the rotational ground state can be initially randomly oriented while, for the rotationally excited molecules, the quantization of the angular momentum \mathbf{L} and the quantization of its projections on a space-fixed axis and on a body-fix axis translate into constraints on the initial orientation effectively aligning the molecule.

Within the rigid rotor approximation, the projection of \mathbf{L} on the reference frame z axis depends only on the choice of the reference frame itself while the projection on the molecular rotational axis depends on the geometry of the molecule. The principal rotational axis of a rigid rotor (here called a , b and c) and the associated moments of inertia (labeled I_A , I_B and I_C from the smallest to the largest) can be obtained from the eigenvectors and the eigenvalues of the inertia tensor \mathbf{I} , respectively. Rigid rotors can be divided to four categories: linear, symmetric, spherical and asymmetric according to the moments of inertia. For a linear rotor, as the H_2 molecule, $I_A \ll I_B = I_C$. Symmetric rotors can be divided to oblate symmetric top (e.g. benzene) for which $I_A = I_B < I_C$ and prolate symmetric top (e.g. methyl-acetate $\text{CH}_3\text{C}\equiv\text{CH}$) for which $I_A < I_B = I_C$. Finally spherical top rotors (e.g. CH_4) shows $I_A = I_B = I_C$ and asymmetric top rotors (e.g. HOD) $I_A < I_B < I_C$. In the following paragraphs the procedure to generate a sample of molecules in a rotationally aligned state is described in detail for an oblate symmetric top molecule as the methane isotopologue CHD_3 . A few details will be also given on how to proceed for an asymmetric top molecule like partially deuterated water (HOD).

Considering an oblate top molecule like CHD_3 , the principal axis (c), associated with the largest moment of inertia I_C , runs through the H atom, the C atom and through the geometrical center of the CD_3 umbrella (Figure 2.1A). The axes

a and b lay in the plane perpendicular to c and are associated with I_A and I_B which are smaller than I_C and of the same magnitude. For CHD_3 a rotational state is defined by the angular momentum \mathbf{L} , by its magnitude:

$$|\mathbf{L}| = \hbar\sqrt{J(J+1)}, \quad (2.32)$$

by its projections on the reference frame z axis:

$$J_z = \hbar M, \quad (2.33)$$

and by its projection on the principal axis c :

$$J_c = \hbar K. \quad (2.34)$$

Here M and K are integers in the range $[-J, +J]$. When the classical analogue of a rotational state is prepared, these projections add constraints to the orientation of the molecules resulting in a certain degree of alignment among the molecules of the sample.

The CHD_3 molecule can be prepared in a given (J, M, K) state according to the following procedure:

- The molecule in its equilibrium geometry is aligned with the principal axis c parallel to the reference frame z which is chosen to be normal to the surface on which the molecule will impinge (Figure 2.1A).
- The rotation in α_1 around the principal axis, which is the first unconstrained degree of freedom, is randomly sampled (Figure 2.1B).
- In order to achieve the projection $\hbar K$ of \mathbf{L} on the principal axis c , the molecule is rotated by:

$$\beta = \cos^{-1}\left(\frac{K}{\sqrt{J(J+1)}}\right). \quad (2.35)$$

Note that the angular momentum \mathbf{L} is still assumed to be aligned with z

(Figure 2.1C).

- The second unconstrained degree of freedom is sampled by randomly fixing the orientation of the principal axis c with respect to the angular momentum \mathbf{L} through the angle α_2 while keeping the projection of \mathbf{L} on c constant (Figure 2.1D).
- The projection $\hbar M$ of the angular momentum \mathbf{L} on the reference frame axis z is then defined, as shown in Figure 2.1E, by rotating both the molecule and the angular momentum by:

$$\phi = \cos^{-1} \left(\frac{M}{\sqrt{J(J+1)}} \right). \quad (2.36)$$

- The last unconstrained degree of freedom is fixed by randomly orienting \mathbf{L} with respect to the reference frame axis z through the rotation α_3 while keeping the projection of \mathbf{L} on z constant. Note that the same random rotation around z is applied to both the angular momentum and the molecule (Figure 2.1F).
- Once the orientation of the molecule and of the angular momentum have been fixed, the rotational component of the velocity \mathbf{v}_{rot} can be computed from:

$$\mathbf{L} = \mathbf{I} \boldsymbol{\omega}_{rot}, \quad (2.37)$$

$$\mathbf{v}_{rot} = \boldsymbol{\omega}_{rot} \times \mathbf{q}, \quad (2.38)$$

where \mathbf{I} is the inertia tensor, $\boldsymbol{\omega}_{rot}$ is the rotational velocity and \mathbf{q} is the vector of the coordinates.

Finally, the total velocity \mathbf{v} and the position \mathbf{q} of each atom of the molecule can be assigned as:

$$\mathbf{v} = \mathbf{v}_{trans} + \mathbf{v}_{rot} + \mathbf{v}_{vib}, \quad (2.39)$$

$$\mathbf{q} = \mathbf{R} \left(\mathbf{q}_0 + \delta \mathbf{q}_{vib} \right)_i, \quad (2.40)$$

where \mathbf{R} is the rotational matrix that aligns the molecule as described above, \mathbf{q}_0 is the equilibrium positions of the atoms with the molecular COM in the origin of the coordinate system and $\delta \mathbf{q}_{vib}$ is the sum of the displacements used to impart the vibrational energy. Note that the rotational and the vibrational velocities need to be rotated according to \mathbf{R} as well. When the molecule is prepared in the desired rovibrational state, it can then be translated to its initial position above the metal surface.

The same strategy can be applied to different molecules considering that a different kind of rotor will introduce different constraints on the initial orientation. For an asymmetric rotor as HOD in our approximate representation, a rotational state is characterized by 4 “quantum numbers”: (J, M, K_a, K_c) . Here J , M , and K_c are the same as observed for CHD_3 and control the magnitude of \mathbf{L} , its projection on z and on the principal axis, respectively. The additional K_a number is related to the projection on another molecular axis and adds an extra constraint on the initial orientation, reducing to 2 the number of randomly sampled DOFs (see Chapter 7).

2.4.2 van der Waals Functionals and Residual Energy

When a vdW correlation functional is used the simulation box needs to be big enough to accommodate the large amount of vacuum between the slab and its 1st periodic image ($\approx 30 \text{ \AA}$) necessary to converge the long range interaction. However, it has been shown for CHD_3 on Ni(111) [7] and on platinum [8] that, to a very good approximation, using a smaller amount of vacuum (e.g., 13 \AA instead of a well-converged value of 30 \AA) affects the energy of the system only as a small upwards shift of the gas-phase level, due to residual interaction with the slab periodic replica, as sketched in Figure 2.2. The residual energy (E_R) is defined as the difference between the energy of the molecule placed away from the surface, i.e. where it sits at the beginning of the simulations (typically 6 \AA), in the cell

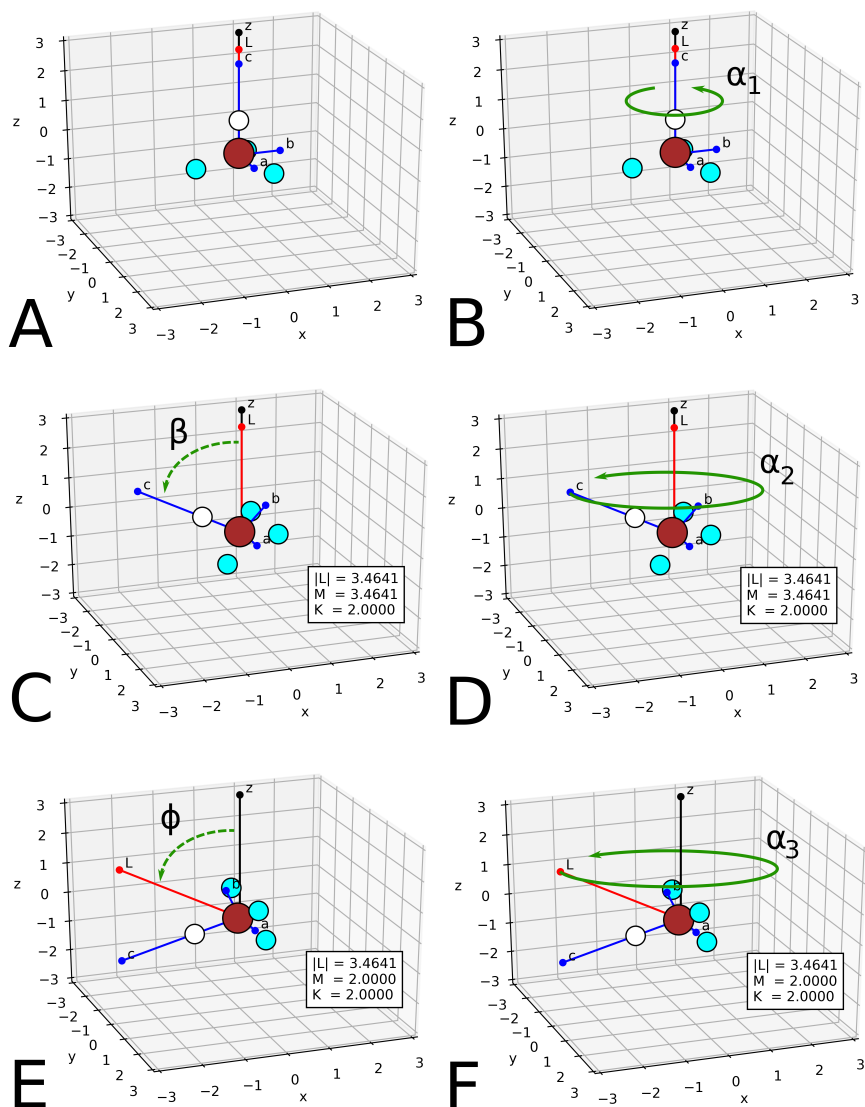


Figure 2.1: Scheme of the rotations needed to prepare the CHD_3 molecule in a generic aligned rotational state ($J = 3, M = 2, K = 2$). The carbon atom is reported in brown, the hydrogen in white and the deuteriums in light blue. The reference frame axis z is reported in black and the molecular axes a, b and c are reported in blue. The angular momentum \mathbf{L} is indicated in red. Dashed green arrows indicate rotations to obtain the correct projections of \mathbf{L} and full green arrows indicate rotations that are sampled randomly. The values on the axes are reported in \AA and $|\mathbf{L}|$ is in atomic units.

with 13 Å and in the one with 30 Å of vacuum:

$$E_R = E_{Z=6\text{Å}}^{13\text{Å}} - E_{Z=6\text{Å}}^{30\text{Å}} \approx \Delta E_b = E_b^{13\text{Å}} - E_b^{30\text{Å}}. \quad (2.41)$$

In order to validate this approximation, E_R has to be the same as the difference in the minimum barrier height (ΔE_b) computed with the two cell sizes ($E_b^{13\text{Å}}$ and $E_b^{30\text{Å}}$, respectively) to within much better than chemical accuracy. In order to correct for the residual interaction in the AIMD simulations the molecules can be assigned an extra translational energy equal to E_R which depends on the system investigated and it is usually on the order of a few of kJ/mol [7, 8, 53]. By imparting this excess energy, the molecules experience an effective barrier (E_b^e) that is approximately equal to the converged barrier height:

$$E_b^e = E_b^{13\text{Å}} - E_R \approx E_b^{30\text{Å}}. \quad (2.42)$$

This implies that the energy barrier converged for the amount of vacuum can be obtained by subtracting E_R from the non-converged barrier. Similarly, the adsorption energies (see Figure 2.2) obtained with the non-converged setup need to be increased by E_R .

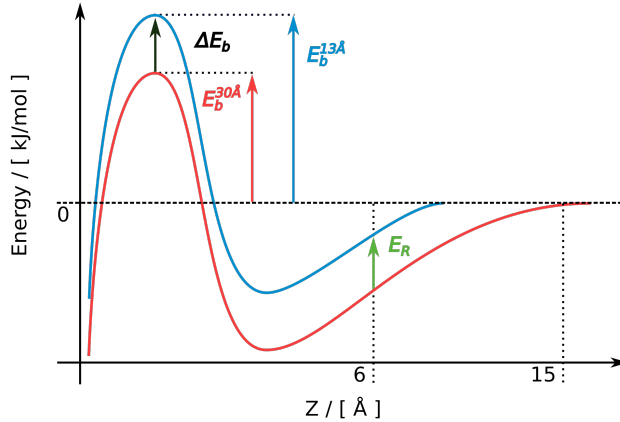


Figure 2.2: Sketch of the barriers considered for a molecule on a metal surface when using a long range functional. The blue and the red curves refer to the 13 Å and to the 30 Å setup, respectively. The barrier heights are shown as arrows in the same color as the related curve. The residual energy (E_R) is reported as a green arrow and the barrier height difference between the two vacuum sizes (ΔE_b) is reported as a black arrow.

2.4.3 Metal Surface Temperature

Since AIMD allows us to treat explicitly all the degrees of freedom, it is important to accurately represent the experimental surface temperature (T_s). Initial velocities and displacements are randomly generated and assigned to the surface atoms according to their vibrational frequencies and sampling a Boltzmann distribution for the desired temperature. This is done by approximating each atom as an independent harmonic oscillator with kinetic energy $K = \frac{1}{2}mv^2$ and potential energy $V = \frac{1}{2}kq^2$.

From the Boltzmann distribution in energy space $f(E)$:

$$f(E) = A \exp(-E/k_b T), \quad (2.43)$$

where k_b is the Boltzmann constant and T is the temperature, we can derive the distributions in the velocity $f(v)$ and in the position $f(q)$ using the expression of K and V and obtaining A as normalization constant:

$$f(v) = \left[\frac{m}{2\pi k_b T} \right]^{\frac{1}{2}} \exp\left(-\frac{mv^2}{2k_b T}\right), \quad (2.44)$$

$$f(q) = \left[\frac{m\omega^2}{2\pi k_b T} \right]^{\frac{1}{2}} \exp\left(-\frac{m\omega^2 q^2}{2k_b T} \right). \quad (2.45)$$

From here it is straightforward to show that $f(v)$ can be rewritten as a Gaussian distribution centered in $\bar{v} = 0$ and with a standard deviation $\sigma_v = \sqrt{\frac{k_b T}{m}}$:

$$f(v | \bar{v}, \sigma_v) = \frac{1}{\sqrt{2\pi\sigma_v^2}} \exp\left(-\frac{(v - \bar{v})^2}{2\sigma_v^2} \right). \quad (2.46)$$

Similarly a Gaussian distribution $f(q | \bar{q}, \sigma_q)$ centered on $\bar{q} = 0$ and with $\sigma_q = \sqrt{\frac{k_b T}{m\omega^2}}$ can be derived for the positions. Here ω can be taken as the vibrational frequency of a surface atom computed by finite differences.

For each atom a random velocity and position are selected in order to sample these Gaussian distributions for the desired surface temperature T_s . This approximation neglects all kind of coupling and therefore, in order to achieve a sound physical description of the surface at the desired temperature, the slab needs to be equilibrated by performing a standard AIMD propagation for 2 ps. Finally any step among the last ps of equilibration can be chosen as initial condition for the trajectories.

Bibliography

- [1] C. Stegelmann, A. Andreasen, and C. T. Campbell, “Degree of Rate Control: How Much the Energies of Intermediates and Transition States Control Rates,” *J. Am. Chem. Soc.*, vol. 131, pp. 8077–8082, 2009.
- [2] G. J. Kroes, “Six-Dimensional Quantum Dynamics of Dissociative Chemisorption of H₂ on Metal Surfaces,” *Prog. Surf. Sci.*, vol. 60, pp. 1–85, 1999.
- [3] G. J. Kroes, “Toward a Database of Chemically Accurate Barrier Heights for Reactions of Molecules with Metal Surfaces,” *J. Phys. Chem. Lett.*, vol. 6, pp. 4106–4114, 2015.
- [4] C. Díaz, E. Pijper, R. A. Olsen, H. F. Busnengo, D. J. Auerbach, and G. J. Kroes, “Chemically Accurate Simulation of a Prototypical Surface Reaction: H₂ Dissociation on Cu(111),” *Science*, vol. 326, pp. 832–834, 2009.
- [5] L. Sementa, M. Wijzenbroek, B. J. van Kolck, M. F. Somers, A. Al-Halabi, H. F. Busnengo, R. A. Olsen, G. J. Kroes, M. Rutkowski, C. Thewes, N. F. Kleimeier, and H. Zacharias, “Reactive Scattering of H₂ from Cu(100): Comparison of Dynamics Calculations Based on the Specific Reaction Parameter Approach to Density Functional Theory with Experiment,” *J. Chem. Phys.*, vol. 138, p. 044708, 2013.
- [6] E. Nour Ghassemi, M. Wijzenbroek, M. F. Somers, and G. J. Kroes, “Chemically Accurate Simulation of Dissociative Chemisorption of D₂ on Pt(111),” *J. Chem. Phys. Lett.*, vol. 683, pp. 329–335, 2017.
- [7] F. Nattino, D. Migliorini, G. J. Kroes, E. Dombrowski, E. A. High, D. R. Killelea, and A. L. Utz, “Chemically Accurate Simulation of a Polyatomic Molecule-Metal Surface Reaction,” *J. Phys. Chem. Lett.*, vol. 7, pp. 2402–2406, 2016.
- [8] D. Migliorini, H. Chadwick, F. Nattino, A. Gutiérrez-González, E. Dombrowski, E. A. High, H. Guo, A. L. Utz, B. Jackson, R. D. Beck, and G. J.

-
- Kroes, “Surface Reaction Barriometry: Methane Dissociation on Flat and Stepped Transition-Metal Surfaces,” *J. Phys. Chem. Lett.*, vol. 8, pp. 4177–4182, 2017.
- [9] F. Nattino, H. Ueta, H. Chadwick, M. E. van Reijzen, R. D. Beck, B. Jackson, M. C. van Hemert, and G. J. Kroes, “Ab Initio Molecular Dynamics Calculations versus Quantum-State-Resolved Experiments on $\text{CHD}_3+\text{Pt}(111)$: New Insights into a Prototypical Gas–Surface Reaction,” *J. Phys. Chem. Lett.*, vol. 5, pp. 1294–1299, 2014.
- [10] A. Groß and A. Dianat, “Hydrogen Dissociation Dynamics on Precovered Pd Surfaces: Langmuir is still Right,” *Phys. Rev. Lett.*, vol. 98, p. 206107, 2007.
- [11] P. Hohenberg and W. Kohn, “Inhomogeneous Electron Gas,” *Phys. Rev.*, vol. 136, pp. B864–B871, 1964.
- [12] W. Kohn and L. J. Sham, “Self-Consistent Equations Including Exchange and Correlation Effects,” *Phys. Rev. B*, pp. A1133–A1138, 1965.
- [13] P. E. Blöchl, “Projector Augmented Wave-Method,” *Phys. Rev. B*, vol. 50, pp. 17953–17979, 1994.
- [14] G. Kresse and D. Joubert, “From Ultrasoft Pseudopotentials to the Projector Augmented-Wave Method,” *Phys. Rev. B*, vol. 59, pp. 1758–1775, 1999.
- [15] F. Bloch, “Bemerkung zur Elektronentheorie des Ferromagnetismus und der elektrischen Leitfähigkeit,” *Z. Phys.*, vol. 57, pp. 545–555, 1929.
- [16] P. A. M. Dirac, “Note on Exchange Phenomena in the Thomas Atom,” *Math. Proc. Camb. Philos. Soc.*, vol. 26, pp. 376–385, 1930.
- [17] D. M. Ceperley and B. J. Alder, “Ground-State of the Electron-Gas by a Stochastic Method,” *Phys. Rev. Lett.*, vol. 45, pp. 566–569, 1980.
- [18] J. P. Perdew, K. Burke, and M. Ernzerhof, “Generalized Gradient Approximation Made Simple,” *Phys. Rev. Lett.*, vol. 77, pp. 3865–3868, 1996.

- [19] J. P. Perdew, K. Burke, and M. Ernzerhof, “Erratum: Generalized Gradient Approximation Made Simple,” *Phys. Rev. Lett.*, vol. 78, p. 1396, 1997.
- [20] B. Hammer, L. B. Hansen, and J. K. Nørskov, “Improved Adsorption Energetics Within Density-Functional Theory Using Revised Perdew-Burke-Ernzerhof Functionals,” *Phys. Rev. B*, vol. 59, pp. 7413–7421, 1999.
- [21] A. Tkatchenko, “Current Understanding of van der Waals Effects in Realistic Materials,” *Adv. Funct. Mater.*, vol. 25, pp. 2054–2061, 2015.
- [22] V. G. Ruiz, W. Liu, E. Zojer, M. Scheffler, and A. Tkatchenko, “Density-Functional Theory with Screened van der Waals Interactions for the Modeling of Hybrid Inorganic-Organic Systems,” *Phys. Rev. Lett.*, vol. 108, p. 146103, 2012.
- [23] F. Furche, “Molecular Tests of the Random Phase Approximation to the Exchange-Correlation Energy Functional,” *Phys. Rev. B*, vol. 64, p. 195120, 2001.
- [24] M. Dion, H. Rydberg, E. Schröder, D. C. Langreth, and B. I. Lundqvist, “Van der Waals Density Functional for General Geometries,” *Phys. Rev. Lett.*, vol. 92, p. 246401, 2004.
- [25] G. Román-Pérez and J. M. Soler, “Efficient Implementation of a van der Waals Density Functional: Application to Double-Wall Carbon Nanotubes,” *Phys. Rev. Lett.*, vol. 103, p. 096102, 2009.
- [26] K. Berland, V. R. Cooper, K. Lee, E. Schroeder, T. Thonhauser, P. Hyldgaard, and B. I. Lundqvist, “van der Waals Forces in Density Functional Theory: a Review of the vdW-DF Method,” *Rep. Prog. Phys.*, vol. 78, p. 066501, 2015.
- [27] Y. Y. Chuang, M. L. Radhakrishnan, P. L. Fast, C. J. Cramer, and D. G. Truhlar, “Direct Dynamics for Free Radical Kinetics in Solution: Solvent Effect on the Rate Constant for the Reaction of Methanol with Atomic Hydrogen,” *J. Phys. Chem. A*, vol. 103, pp. 4893–4909, 1999.

-
- [28] M. Wijzenbroek and G. J. Kroes, “The Effect of the Exchange-Correlation Functional on H₂ Dissociation on Ru(0001),” *J. Chem. Phys.*, vol. 140, p. 084702, 2014.
- [29] P. M. Hundt, B. Jiang, M. E. van Reijzen, H. Guo, and R. D. Beck, “Vibrationally Promoted Dissociation of Water on Ni(111),” *Science*, vol. 344, pp. 504–507, 2014.
- [30] F. Nattino, C. Díaz, B. Jackson, and G. J. Kroes, “Effect of Surface Motion on the Rotational Quadrupole Alignment Parameter of D₂ Reacting on Cu(111),” *Phys. Rev. Lett.*, vol. 108, p. 236104, 2012.
- [31] P. Nieto, D. Farías, R. Miranda, M. Luppi, E. J. Baerends, M. F. Somers, M. J. T. C. van der Niet, R. A. Olsen, and G. J. Kroes, “Diffractive and Reactive Scattering of H₂ from Ru(0001): Experimental and Theoretical Study,” *Phys. Chem. Chem. Phys.*, vol. 13, pp. 8583–8597, 2011.
- [32] I. M. N. Groot, H. Ueta, M. J. T. C. van der Niet, A. W. Kleyn, and L. B. F. Juurlink, “Supersonic Molecular Beam Studies of Dissociative Adsorption of H₂ on Ru(0001),” *J. Chem. Phys.*, vol. 127, p. 244701, 2007.
- [33] F. Nattino, D. Migliorini, M. Bonfanti, and G. J. Kroes, “Methane Dissociation on Pt(111): Searching for a Specific Reaction Parameter Density Functional,” *J. Chem. Phys.*, vol. 144, p. 044702, 2016.
- [34] M. Wijzenbroek, D. M. Klein, B. Smits, M. F. Somers, and G. J. Kroes, “Performance of a Non-Local van der Waals Density Functional on the Dissociation of H₂ on Metal Surfaces,” *J. Phys. Chem. A*, vol. 119, pp. 12146–12158, 2015.
- [35] J. P. Perdew, A. Ruzsinszky, J. M. Tao, V. N. Staroverov, G. E. Scuseria, and G. I. Csonka, “Prescription for the Design and Selection of Density Functional Approximations: More constraint Satisfaction with Fewer Fits,” *J. Chem. Phys.*, vol. 123, p. 062201, 2005.

- [36] H. Chadwick, A. Gutiérrez-González, and R. D. Beck, “Quantum State Resolved Molecular Beam Reflectivity Measurements: CH₄ Dissociation on Pt(111),” *J. Chem. Phys.*, vol. 145, p. 174707, 2016.
- [37] D. A. King and M. G. Wells, “Molecular-Beam Investigation of Adsorption Kinetics on Bulk Metal Targets - Nitrogen on Tungsten,” *Surf. Sci.*, vol. 29, pp. 454–482, 1972.
- [38] B. Jiang, R. Liu, J. Li, D. Q. Xie, M. H. Yang, and H. Guo, “Mode Selectivity in Methane Dissociative Chemisorption on Ni(111),” *Chem. Sci.*, vol. 4, pp. 3249–3254, 2013.
- [39] A. Farjamnia and B. Jackson, “The Dissociative Chemisorption of Water on Ni(111): Mode- and Bond-Selective Chemistry on Metal Surfaces,” *J. Chem. Phys.*, vol. 142, p. 234705, 2015.
- [40] S. Nave and B. Jackson, “Methane Dissociation on Ni(111): The Role of Lattice Reconstruction,” *Phys. Rev. Lett.*, vol. 98, p. 173003, 2007.
- [41] M. Blanco-Rey, J. I. Juaristi, R. Díez Muiño, H. F. Busnengo, G. J. Kroes, and M. Alducin, “Electronic Friction Dominates Hydrogen Hot-Atom Relaxation on Pd(100),” *Phys. Rev. Lett.*, vol. 112, p. 103203, 2014.
- [42] B. Jackson and S. Nave, “The Dissociative Chemisorption of Methane on Ni(100): Reaction Path Description of Mode-Selective Chemistry,” *J. Chem. Phys.*, vol. 135, p. 114701, 2011.
- [43] X. G. Wang and E. L. Sibert, “A Nine-Dimensional Perturbative Treatment of the Vibrations of Methane and its Isotopomers,” *J. Chem. Phys.*, vol. 111, pp. 4510–4522, 1999.
- [44] G. Czako and J. M. Bowman, “Dynamics of the Reaction of Methane with Chlorine Atom on an Accurate Potential Energy Surface,” *Science*, vol. 334, pp. 343–346, 2011.

-
- [45] J. R. Manson, “Energy Transfer to Phonons in Atom and Molecule Collisions with Surfaces,” in *Handbook of Surface Science* (E. Hasselbrink and B. I. Lundqvist, eds.), vol. 3, pp. 53–93, Elsevier, 2008.
- [46] J. R. Manson, “Inelastic-Scattering from Surfaces,” *Phys. Rev. B*, vol. 43, pp. 6924–6937, 1991.
- [47] J. R. Manson, “Multiphonon Atom-Surface Scattering,” *Comput. Phys. Commun.*, vol. 80, pp. 145–167, 1994.
- [48] W. L. Hays, *Statistics, 3rd edn.* Holt: Rinehart and Winston, 1981.
- [49] K. Shakouri, J. Behler, J. Meyer, and G. J. Kroes, “Accurate Neural Network Description of Surface Phonons in Reactive Gas-Surface Dynamics: $\text{N}_2 + \text{Ru}(0001)$,” *J. Phys. Chem. Lett.*, vol. 8, pp. 2131–2136, 2017.
- [50] L. B. F. Juurlink, D. R. Killelea, and A. L. Utz, “State-Resolved Probes of Methane Dissociation Dynamics,” *Progr. Surf. Sci.*, vol. 84, pp. 69–134, 2009.
- [51] H. A. Michelsen and D. J. Auerbach, “A Critical Examination of Data on the Dissociative Adsorption and Associative Desorption of Hydrogen at Copper Surfaces,” *J. Chem. Phys.*, vol. 94, pp. 7502–7520, 1991.
- [52] H. Chadwick, A. Gutiérrez-González, D. Migliorini, R. D. Beck, and G. J. Kroes, “Incident Angle Dependence of CHD_3 Dissociation on the Stepped $\text{Pt}(211)$ Surface,” *J. Phys. Chem. C*, vol. 122, pp. 19652–19660, 2018.
- [53] D. Migliorini, F. Nattino, A. K. Tiwari, and G. J. Kroes, “HOD on $\text{Ni}(111)$: Ab Initio Molecular Dynamics Prediction of Molecular Beam Experiments,” *J. Chem. Phys.*, vol. 149, p. 244706, 2018.

